



## Research paper

# Digital Volume Correlation for large deformations of soft tissues: Pipeline and proof of concept for the application to breast *ex vivo* deformations

T. Lavigne<sup>a</sup>, A. Mazier<sup>a</sup>, A. Perney<sup>a,d</sup>, S.P.A. Bordas<sup>a,e,\*</sup>, F. Hild<sup>c</sup>, J. Lengiewicz<sup>a,b</sup>

<sup>a</sup> Institute of Computational Engineering, Department of Engineering, University of Luxembourg, 6, avenue de la Fonte, Esch-sur-Alzette, L-4364, Luxembourg

<sup>b</sup> Institute of Fundamental Technological Research, Polish Academy of Sciences (IPPT PAN), Pawinskiego 5B, Warsaw, 02-106, Poland

<sup>c</sup> University Paris-Saclay, CentraleSupélec, ENS Paris-Saclay, CNRS, LMPS-Laboratoire de Mécanique Paris-Saclay, 4 avenue des Sciences, 91190, Gif-sur-Yvette, France

<sup>d</sup> Centre des Matériaux, Mines ParisTech, PSL University, 63-65 Rue Henri Auguste Desbrières, Corbeil-Essonnes, 91100, France

<sup>e</sup> Visiting professor at Department of Medical Research, China Medical University Hospital, China Medical University, Taichung, Taiwan

## ARTICLE INFO

## Keywords:

Digital Volume Correlation  
Elastic regularization  
Hard/soft tissues  
Large displacements  
Kinematic fields  
X-ray tomography

## ABSTRACT

Being able to reposition tumors from prone imaging to supine surgery stances is key for bypassing current invasive marking used for conservative breast surgery. This study aims to demonstrate the feasibility of using Digital Volume Correlation (DVC) to measure the deformation of a female quarter thorax between two different body positioning when subjected to gravity. A segmented multipart mesh (bones, cartilage and tissue) was constructed and a three-step FE-based DVC procedure with heterogeneous elastic regularization was implemented. With the proposed framework, the large displacement field of a hard/soft breast sample was recovered with low registration residuals and small error between the measured and manually determined deformations of phase interfaces. The present study showed the capacity of FE-based DVC to faithfully capture large deformations of hard/soft tissues.

## 1. Introduction

According to the World Health Organization, “as of the end of 2020, there were 7.8 million women alive who were diagnosed with breast cancer in the past 5 years, making it the world’s most prevalent cancer.” In breast cancer treatment, surgery is one of the most common practices (DeSantis et al., 2019). In breast-conserving surgery, the imaging procedure (*i.e.*, MRI) is conducted in prone configurations while surgery is performed in supine stance (Rajagopal, 2007; Rajagopal et al., 2010; Georgii et al., 2016; Mazier et al., 2021). Thus, the surgeon has to mentally predict tumor deformations or use invasive markings such as harpoons or radioactive markers to follow tumor motions. Numerical methods may bypass the marking step, which induces additional uncertainties of the procedure. Biomechanical simulations may predict such complex tumor deformations yet require patient-specific data (*e.g.*, material properties, organ geometry, loading and boundary conditions).

Accurately characterizing large and complex deformation fields, as is likely to occur with soft tissues, is challenging and several studies tackled such problem (Gavaghan et al., 2008; Rajagopal et al., 2008; Lee et al., 2010). Few of them presented satisfying results or only

validated surface displacement fields (Eiben et al., 2016). Most of the time, these methods solely rely on the finite element method combined with free-form deformers (*e.g.*, B-spline warping of images) or are lacking clinical validation. In this work, it is proposed to measure 3D displacement fields based on *ex vivo* medical images. Usually, women diagnosed with breast cancer undergo MRI and/or mammography, which are the starting point of surgical procedures (Gavaghan et al., 2008; Lee et al., 2010; Duraes et al., 2019). Digital Image Correlation (DIC), stereocorrelation or Digital Volume Correlation (DVC) use similar inputs and provide experimentally measured displacement fields of surfaces or in the bulk (Sutton et al., 2009; Sutton, 2013). DVC may allow for the development of patient-specific models to estimate tumor motions due to changes in stance between imaging and intra-operative configurations, and will drastically enrich the surgeon’s knowledge, thereby helping procedure planning. Previous studies showed the possibility of using DIC and stereovision principles on breasts to measure surface stretches. Khatam et al. (2015) manually tracked drawn surgical markers and then assessed surface stretches. Such approaches do not give access to fields in the breast bulk, especially internal strain maps.

DVC is an experimental technique that allows for the measurement of displacement fields in three dimensions (Bay et al., 1999). It is

\* Corresponding author at: Institute of Computational Engineering, Department of Engineering, University of Luxembourg, 6, avenue de la Fonte, Esch-sur-Alzette, L-4364, Luxembourg.

E-mail address: [stephane.bordas@alum.northwestern.edu](mailto:stephane.bordas@alum.northwestern.edu) (S.P.A. Bordas).

<https://doi.org/10.1016/j.jmbbm.2022.105490>

Received 1 July 2022; Received in revised form 21 September 2022; Accepted 26 September 2022

Available online 30 September 2022

1751-6161/© 2022 The Authors. Published by Elsevier Ltd. This is an open access article under the CC BY license (<http://creativecommons.org/licenses/by/4.0/>).

used to extract strain maps in solid mechanics, but mostly for stiff materials (Bay, 2008; Buljac et al., 2018a) such as bones (Bay et al., 1999; Liu and Morgan, 2007; Benoit et al., 2009; Hussein et al., 2012; Gillard et al., 2014; Peña Fernández et al., 2022; Palanca et al., 2022; Wu et al., 2022) and often relies on the hypothesis of infinitesimal strains between two successive configurations to ensure convergence. DVC is gaining interest in the biomechanical field (Palanca et al., 2015; Disney et al., 2018; Dall'Ara et al., 2022). Recently, DVC was applied to study the spine (Tozzi et al., 2017; Ruspi et al., 2019). Several works used DVC to map strain fields for arteries (Santamaria et al., 2020), tendons (Sartori et al., 2021), intervertebral disks (Disney et al., 2019, 2022), tissue interfaces with prosthetics (Rankin et al., 2020) or even the mitral valve (Pierce et al., 2016). Optical coherence elastography/tomography techniques (e.g., for the identification of elastic properties) based on DVC with 3D infinitesimal strain measurements were performed *ex vivo* on mesoscopic (i.e., millimetric regions of interest) human (Nahas et al., 2013) and chicken (Meng et al., 2019) breast tissues. As DVC requires high quality images to properly converge, the regions of interest are usually of the order of centimeters (due to technical limitations of setups). A breast subjected to gravity from prone to supine positions undergoes large deformations, which calls for registrations of large regions of interest via DVC. As MRIs are expensive and uncomfortable, one envisions that only two MRI scans would be performed. Therefore, two main challenges arise when dealing with breasts, namely, the strain levels may become high between two consecutive acquisitions (i.e., they do not satisfy the small strain hypothesis) and the dimension of the region of interest may be large.

The following study is a proof of concept that aims to prove the feasibility of using DVC to measure experimental displacement fields for a breast subjected to its weight when imaged in two different angular configurations wrt. gravity. First, the image acquisition, processing and mesh generation procedures are described. Then, DVC and heterogeneous regularization are recalled. Next, a three-step DVC pipeline is discussed to measure the large amplitude deformations of the studied breast. Last, the results are presented and discussed.

## 2. Material and methods

### 2.1. Image acquisition

A left quarter of a thorax (of size  $0.27\text{ m} \times 0.26\text{ m} \times 0.06\text{ m}$ ) was extracted from a female corpse. Fifteen biomarkers were put on the surface and inside the breast to provide some displacement information (Fig. 1(a)). These markers were placed by the medical team and assumed rigidly attached to the sample using an adhesive surface. The breast was injected with physiological serum to get closer to an *in vivo* configuration and to mimic its initial mechanical properties.

The medical images were acquired at Arnaud de Villeneuve Hospital (Montpellier, France) by Prof. Guillaume Captier and AnatoScope company. The use for research purposes of body donations and removals was in accordance with French law according to the decree of April 27, 2022. The patient-specific geometry was imaged via micro-computed tomography using an RX Solutions scanner with a  $0.34\text{ mm}$  resolution. This resolution may be considered as low-quality for tomographies as the X-ray scanner allows for values down to  $15\text{ }\mu\text{m}$ . The choice of such resolution was motivated by 3 reasons. First, high-resolution acquisitions are usually lengthy (i.e., between 3 to 4 h). Second, the cadaver tissues will quickly degrade, thereby preventing from performing a second acquisition. Last, the present CT-scans and clinical MRI images have similar resolutions.

Two different configurations were acquired, namely,  $-45^\circ$  and  $-60^\circ$  in the axial plane with no intermediate states (Fig. 1(b,c)). The angles were reached using a inclined wooden support on which the breast was fastened using four plastic straps to be compatible with medical imaging procedures. The assembly was manually moved to go from

one configuration to the other. The hardware parameters are reported in Appendix A. As the images were not acquired for DVC purposes, different (Tukey) filtering values were used resulting in variable gray level ranges.

### 2.2. Mesh generation

Based on the gray levels (Fig. 2(a)) and anatomic knowledge, three entities (phases) were created, namely, breast tissue, bones, and cartilage. A growth from seeds algorithm was manually initialized (i.e., several slices in each  $X, Y, Z$  direction of the volume were manually “painted” so the algorithm was able to identify regions and gray levels belonging to each individual phase) within the 3D Slicer software (Fedorov et al., 2012). The result was smoothed, thereby allowing for mesh generations without too small interface segments as nodes in different phases had to coincide on interfaces to enforce kinematic compatibility. Last, an artificial outer layer (15 voxel (vx) thick) was added to the tissue, see Fig. 2(b). This “artificial skin” was added to help DVC register the external surface. Each mask was converted into a sub-mesh and the considered mesh was the coarsest that was obtained using ScanIP Simpleware software. With such mesh, sub-voxel elements were avoided.

Fig. 2(c) shows the resulting volumetric meshes and screenshots of Simpleware software, courtesy of Synopsys. The mesh was composed of 41,454 linear tetrahedra with a characteristic element length of  $9.3 \pm 2.8\text{ vx}$  (i.e.,  $3.2 \pm 0.9\text{ mm}$ ). To avoid too small elements, 25 of them with length less than 3 vx were deleted.

### 2.3. Regularized digital volume correlation

#### 2.3.1. Digital volume correlation

DVC relies on the conservation of gray levels upon transformations between two scanned configurations. The cost function  $\Phi_c^2$  to be minimized in global (e.g., FE-based) DVC is generally expressed as (Buljac et al., 2018a)

$$\Phi_c^2 = \sum_{ROI} (I_0(\mathbf{x}) - I_t(\mathbf{x} + \mathbf{u}(\mathbf{x})))^2 \quad (1)$$

where  $\mathbf{x}$  is the position of any voxel in the reference configuration,  $\mathbf{u}(\mathbf{x})$  the corresponding continuous displacement vector, and ROI the Region of Interest. The gray levels corresponding to the 3D image of the reference configuration are denoted by  $I_0$ , and those of the deformed configuration  $I_t$ .

In the present case, FE-based DVC was considered with 4-noded tetrahedra (i.e., T4 elements, Hild et al., 2016). The ROI to be registered during the minimization procedure was defined by the considered mesh (Fig. 2(c)). Consequently, the unknowns were the nodal displacements gathered in the column vector  $\{\mathbf{v}\}$  such that

$$\mathbf{u}(\mathbf{x}) = \sum_i v_i \mathbf{N}_i^{T4}(\mathbf{x}) \quad (2)$$

where  $\mathbf{N}_i^{T4}$  denotes the vectorial shape functions of T4 elements. A modified Gauss–Newton scheme was used to minimize  $\Phi_c^2$  with respect to the sought nodal displacements  $\{\mathbf{v}\}$  (Hild et al., 2016)

$$\{\mathbf{v}\}^* = \arg \min_{\{\mathbf{v}\}} \Phi_c^2(\{\mathbf{v}\}) \quad (3)$$

which leads to iteratively solving linear systems of equations

$$[\mathbf{H}]\{\delta\mathbf{v}\} = \{\mathbf{h}\} \quad (4)$$

where  $[\mathbf{H}]$  is the DVC Hessian matrix,  $\{\mathbf{h}\}$  the residual vector, and  $\{\delta\mathbf{v}\}$  the correction nodal displacement vector.

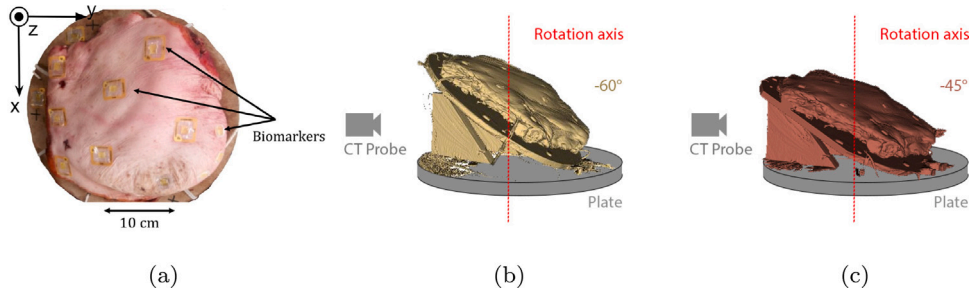


Fig. 1. (a) Left quarter of a female thorax (0.27 m × 0.26 m × 0.06 m in size) injected with physiological serum and fastened to a wooden plate using plastic straps. Fifteen biomarkers were placed on the surface and inside the breast. -60° (b) and -45° (c) positions in the CT-scanner for the studied configurations.

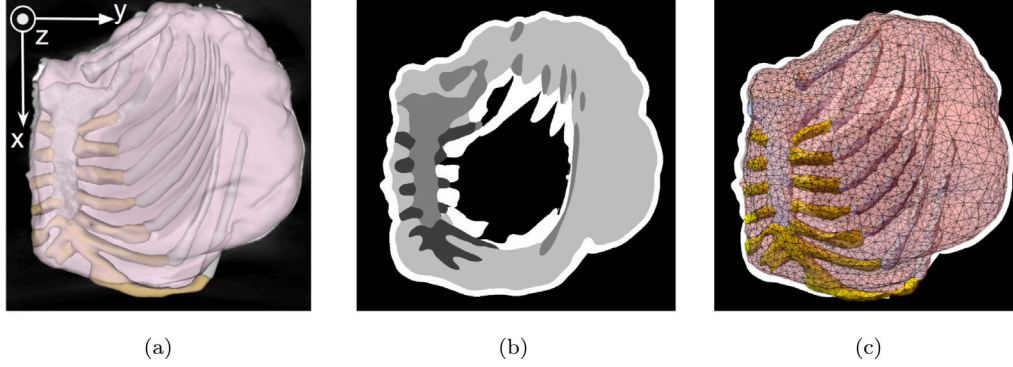


Fig. 2. Phase-based mesh construction of the -60° configuration in the axial plane. (a) Phase segmentation (tissue in pink, bones in white and cartilage in yellow) shown on the original scan. (b) Section of a segmented image with the different phases and the artificial skin layer that was added. (c) Phase-based mesh (courtesy of Synopsys) is shown on the original scan.

### 2.3.2. Heterogeneous regularization

As noted in Section 2.1, the images were not originally acquired for DVC purposes. In particular, the gray level contrast was not optimal. To overcome this issue, mechanical regularization was considered. It consists in adding a penalty term to mitigate displacement fluctuations. In regularized DVC, equilibrium is enforced at the local level by introducing a cost function based on the equilibrium gap (in the absence of body forces) (Claire et al., 2004)

$$[\mathbf{K}]\{\mathbf{v}\} = \{\mathbf{f}_{\text{res}}\} \quad (5)$$

where  $[\mathbf{K}]$  is the stiffness matrix, and  $\{\mathbf{f}_{\text{res}}\}$  the residual force vector. The principle of regularization is to supplement the minimized cost function with the following penalty term

$$\Phi_m^2 = \|\{\mathbf{f}_{\text{res}}\}\|^2 = \{\mathbf{v}\}^T [\mathbf{K}]^T [\mathbf{K}] \{\mathbf{v}\} \quad (6)$$

One may note that the DVC Hessian matrix  $[\mathbf{H}]$  is a 0th order operator with respect to displacements (i.e.,  $[\mathbf{H}]$  depends on the shape functions  $N_i^{T4}$  themselves, and not on any spatial derivative), and  $[\mathbf{K}]$  is a second order operator (Mendoza et al., 2019); thus  $[\mathbf{K}]^T [\mathbf{K}]$  is a fourth-order operator. To have dimensional consistency between  $\Phi_c^2$  and  $\Phi_m^2$ , a regularization length  $\ell_{\text{reg}}$  is defined so that the regularization weight  $w_m \propto \ell_{\text{reg}}^4$ . The total cost function  $\Phi_{\text{tot}}^2$

$$\Phi_{\text{tot}}^2 = \Phi_c^2 + w_m \Phi_m^2 \quad (7)$$

was minimized iteratively (Hild and Roux, 2012). Convergence was reached when the L2-norm of the displacement corrections becomes less than  $10^{-2}$  vx.

In the present study, the ROI covered three different materials (i.e., soft tissue, cartilage, and bones). To account for the fact that their elastic properties were very different, heterogeneous regularization was utilized (Tsitova et al., 2021). As a consequence, each element  $e$  was assigned an elastic contrast  $C^e$  whose value was the ratio of the Young's modulus of the phase it belonged to divided by that of the soft tissue. Thus,  $C^e > 1$  corresponds to a phase stiffer than the soft tissue.

The regularization length,  $\ell_{\text{reg}}$ , scales with the square root of the elastic contrast  $C^e$  (Naylor et al., 2019). For example, if  $C^e = 100$ , then the regularization length is ten times higher (i.e.,  $\sqrt{100}$  factor) for the considered element in comparison to the tissue elements. In all the analyses reported herein, the regularization lengths refer to the softest phase.

A convergence study was carried out to determine the best regularization length. Let us refer to the bone with the index  $\bullet_b$ , cartilage with the index  $\bullet_c$ , and to tissue with the index  $\bullet_t$ . The bone Young's modulus was found to vary between 5 to 50 GPa (Rho et al., 1993; Hunt et al., 1998; Seedhom et al., 2004), and that of cartilage from 8 to 40 MPa (Forman and Kent, 2011; Huwe et al., 2018; Griffin et al., 2020). Breasts are made of different materials such as adipose, fibroglandular, skin, or fascia tissues. In addition to a wide variability between patients, the differences between *in vivo/ex vivo* or compression/tension mechanical tests give a large range of Young's moduli ranging between 0.2 to 28 kPa (Payan and Ohayon, 2017; Míra et al., 2018). Therefore, the elastic contrasts were set to  $C_b = 10^6$ ,  $C_c = 10^4$  and  $C_t = 1$ . Comparisons were also performed to results with two other contrasts, namely,  $C_b = 10^3$ ,  $C_c = 10^2$ ,  $C_t = 1$  and  $C_b = C_c = C_t = 1$  (i.e., homogeneous properties).

### 2.3.3. DVC steps to measure breast deformation

Regularized DVC was applied to measure breast deformation between -60° axial to -45° axial configurations. The analysis consisted of the following three steps.

For the first step, an initial evaluation of the mean deformation gradient tensor,  $\mathbf{F}$ , was obtained, which was based on the motion of  $m = 15$  biomarkers. They were manually identified while segmenting the scans. For each configuration, their position was measured as the geometric barycenter of their segmentation. Therefore, one may consider that the resulting positions include some user uncertainty resulting from the segmentation procedure. This first step corresponds

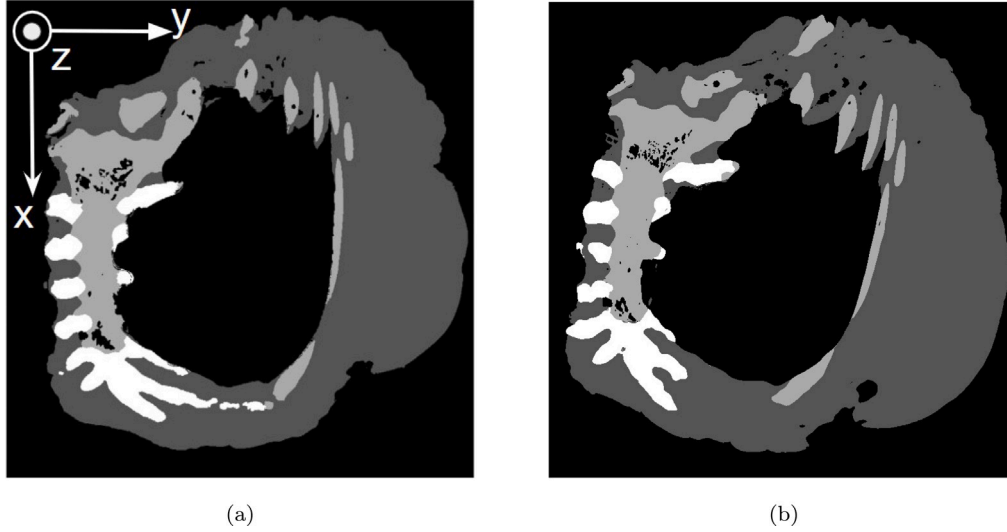


Fig. 3. Sections of segmented volumes corresponding to (a)  $-60^\circ$  and (b)  $-45^\circ$  configurations. Phase-based images were created for the second DVC step (i.e., cartilage in white, bones in light gray, tissue in dark gray and air in black). The phase of confined air was included.

to current practices in which markers are put on the external surface of the breast, and their motions are sought for tumor repositioning.

Let  $\mathbf{x}_m$  denote the position of the  $m$ th marker in the reference configuration, and  $\mathbf{x}_m + \mathbf{u}_m$  its position in the deformed configuration. Considering the deformation gradient tensor  $\mathbf{F}$ , the translation vector  $\mathbf{t}$ , and the second order identity tensor  $\mathbf{I}$ , the approximated field  $\mathbf{u}_a$  reads

$$\mathbf{u}_a(\mathbf{x}_m, \mathbf{F}, \mathbf{t}) = (\mathbf{F} - \mathbf{I})\mathbf{x}_m + \mathbf{t} \quad (8)$$

where the components of  $\mathbf{F}$  and  $\mathbf{t}$  were obtained by least squares minimization

$$[\mathbf{F}^*, \mathbf{t}^*] = \arg \min_{\mathbf{F}, \mathbf{t}} \|\mathbf{u}_m - \mathbf{u}_a(\mathbf{x}_m, \mathbf{F}, \mathbf{t})\|^2 \quad (9)$$

For the second step, a better approximation of the initial displacement field was computed with homogeneous regularized DVC applied to the segmented images created for each configuration (Fig. 3) including internal air. Because the histograms of the raw images were not fully conserved, using such images allowed the gray levels to be made identical for each segmented phase. This DVC step was initialized by the marker-based displacement estimate. No elastic contrast was considered to allow for the correct positioning of the bones. Given the fact that the three phases had uniform gray levels, the gray level contrast (i.e., gradient of image) was nonzero only for a very limited number of voxels (i.e., at interfaces between phases). This property leads to very steep cost functions about the optimal solution. Blurring the volume smoothens the cost function and induces faster convergence of the Newton-based minimization scheme. Thus to improve convergence, the two volumes were blurred (with a Gaussian filter with a radius of 3 vx).

For the third step, the previously measured displacement field was used to initialize the heterogeneous regularized DVC calculation on the original volumes (Fig. 4), with no filtering of the gray levels. The elastic contrasts were set to the values given in Section 2.3.2. The regularization length was set according to the convergence study (Appendix B).

While the gray level residuals  $\rho(\mathbf{x}) = I_0(\mathbf{x}) - I_t(\mathbf{x} + \mathbf{u}(\mathbf{x}))$  of DVC analyses provide a quality indicator for the measured displacement field (see Eq. (1)), the Root Mean Square Error (RMSE) was used as a metric for evaluating the trustworthiness of surface displacements.

$$\text{RMSE}^2 = \frac{1}{N} \sum_{i=1}^N (\mathbf{x}_i^{\text{DVC}} - \mathcal{P}^{\text{seg}}(\mathbf{x}_i^{\text{DVC}}))^2 \quad (10)$$

For each phase of both initial and deformed configurations, a surface (STL) mesh was generated from the volumetric mesh by identifying

the boundary elements. Then, the measured displacement field was applied to the initial surface nodes. For each phase, the error between the assessed  $N$  deformed nodes from DVC  $\mathbf{x}^{\text{DVC}}$  and the refined mesh resulting from the segmentation of the deformed image  $\mathcal{M}^{\text{seg}}$  was computed as the root mean square error (RMSE). As the meshes did not have the same number of nodes, a projection operator  $\mathcal{P}^{\text{seg}}$  of the DVC deformed nodes onto  $\mathcal{M}^{\text{seg}}$  was assessed using an Iterative Closest Point (ICP) algorithm (Besl and McKay, 1992).

#### 2.3.4. Uncertainty quantification

As pointed out above, the imaging conditions were not optimal for DVC purposes and thus may degrade the measurement uncertainties. Furthermore, common practice requires at least two repeat scans to be acquired to quantify kinematic uncertainties *a priori* (Buljac et al., 2018b,a). In the present case, no repeat scan was performed. Thus another (*a posteriori*) route was followed. At the end of any global DVC analysis, the quality of registration is probed by analyzing the gray level residuals  $\rho$ , which contain information about acquisition noise and artifacts, as well as indications about the trustworthiness of the selected kinematic bases (Hild et al., 2015; Buljac et al., 2018a). It was thus decided to artificially create a new volume by applying a 0.5 vx translation along all three Cartesian coordinates to the reference volume. White Gaussian noise was also added (Fig. 5(b)), whose standard deviation  $\sigma_\rho$  was that of the gray level residuals corresponding to the result of the DVC analysis that was deemed the most trustworthy in the sequel. This volume was correlated with the reference volume (Fig. 5(a)). The displacement uncertainties correspond to the standard deviations of nodal displacements in each direction. Similarly, the strain uncertainties were assessed as the standard deviations of elementary strains. As regularized DVC was carried out, the fine mesh was not altered but the regularization length  $\ell_{\text{reg}}$  was varied to assess standard uncertainties (Leclerc et al., 2011; Taillandier-Thomas et al., 2014).

### 3. Results and discussion

#### 3.1. DVC results

In the following results, the mean element size was equal to 10 voxels, and the mean spatial resolution was 17 voxels (the physical voxel size was 0.34 mm).

The marker-based displacement field was computed and applied to the mesh as an initial guess (Fig. 6), which provided a good approximation to recover the overall shape of the sample in the deformed



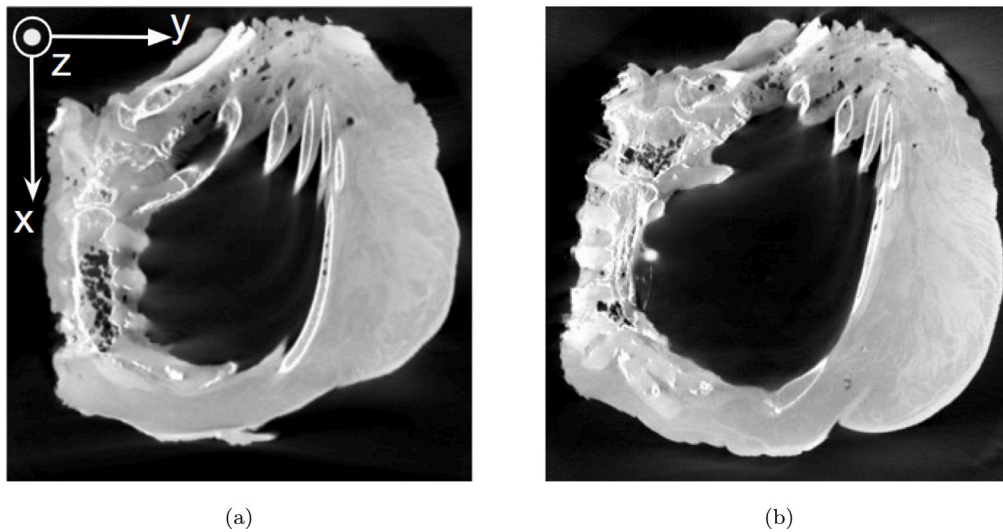


**Fig. 4.** Sections of  $-60^\circ$  (a) and  $-45^\circ$  (b) configurations obtained with an RX-Solutions CT-scanner (voxel size of 0.34 mm) in the axial plane. These volumes were used during the third step of the DVC procedure.

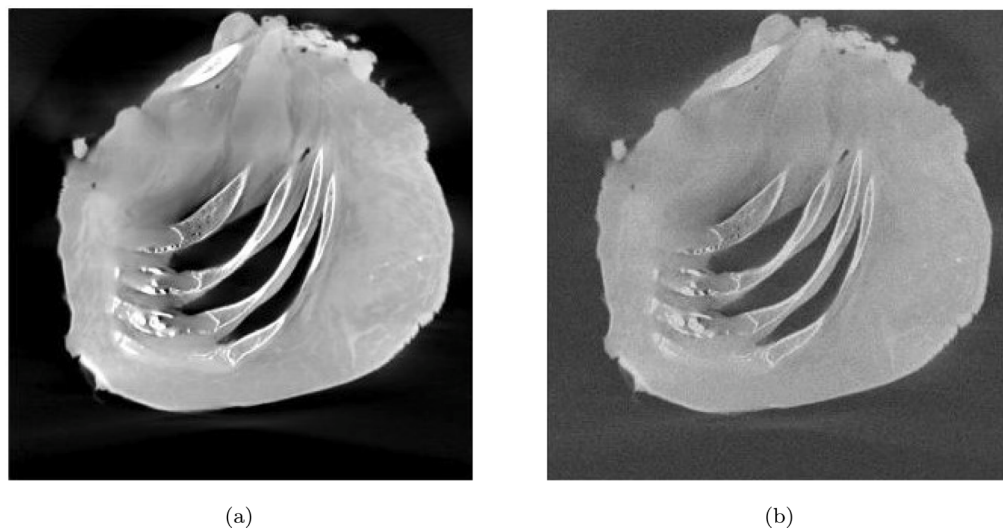


**Fig. 5.** Sections of  $-60^\circ$  original volume (a) and translated volume (b) corrupted with white Gaussian noise whose standard deviation was equal to 18.3 gray levels.

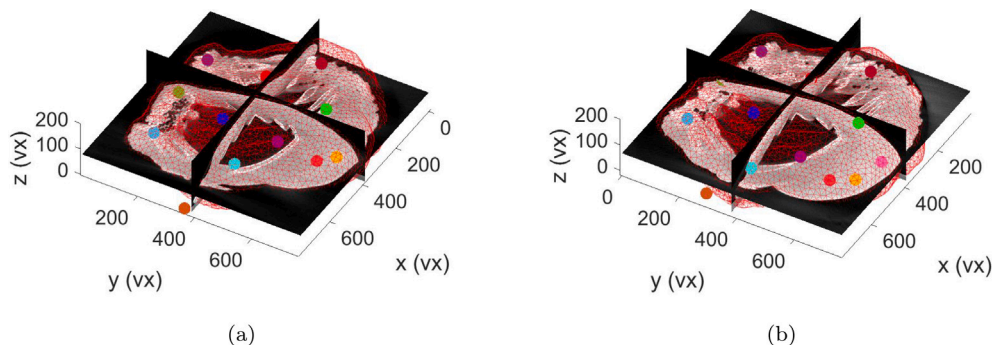


**Fig. 6.** (a) Reference ( $-60^\circ$ ) and (b) deformed ( $-45^\circ$ ) meshes based on the marker motions. The wireframe meshes are superimposed over orthoslices of their respective volumes. The biomarkers are shown as colored disks.

configuration. Because the biomarkers were mainly placed on the surface, the initial guess suffered from inaccuracies in the bulk (e.g., near bones) and led to high RMS residual (63 gray levels).

This first estimate served as initialization for the DVC analysis between the segmented images (for which the gray level distribution

was almost the same (Fig. 7(b))). Therefore, gray level conservation was enforced. The regularization length was set to 35 vx to properly converge (i.e., only 48 DVC iterations were needed). The use of these segmented images allowed for further reducing the gray level residuals (Fig. 7(b)). The final RMS residual was 10.6 gray levels (Fig. 7), which

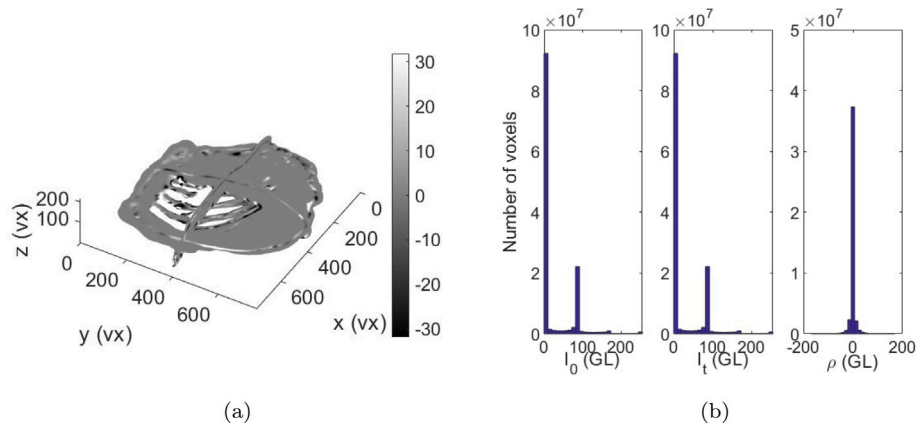


Fig. 7. (a) Gray level residuals are shown within the region of interest defined by the considered mesh. (b) From left to right: gray level histograms of the reference volume  $I_0$ , deformed volume  $I_t$ , and DVC residuals  $\rho$  shown in sub-figure (a).

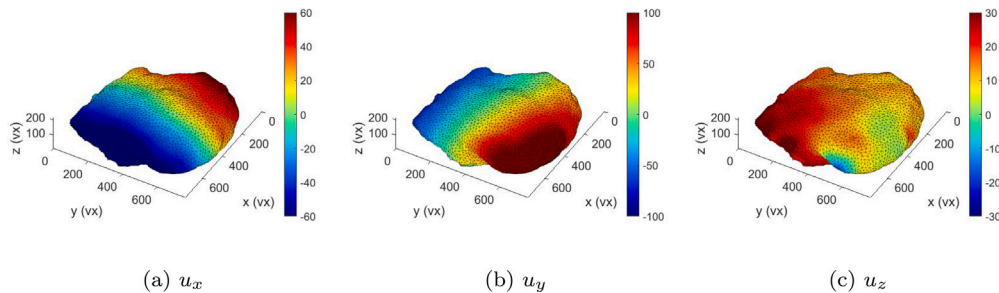


Fig. 8. Displacement field expressed in voxels (1 vx  $\equiv$  0.34 mm) for the DVC analysis on the segmented images. (a)  $u_x$ , (b)  $u_y$  and (c)  $u_z$  components plotted on the deformed mesh.

is deemed low given the complexity of the deformation and acquisition conditions. It is worth noting that the initial RMS level was equal to 62.7 gray levels, which proves that the current practice (*i.e.*, first step) was not sufficient for a precise determination of the tumor position.

Fig. 8 shows the measured displacement field. The tissue phase shifted downward, thereby creating an inframammary fold (Fig. 11(d)). Thanks to the segmented images, this complex configuration could be recovered. Adding the artificial skin layer was a key step to ensure tracking of the interface between the tissue and air. Without such gray level contrast, the procedure could have converged to the wrong positions. However, this result is only the first approximation as no gray level contrast existed inside each phase (Fig. 3). It is worth noting that the displacement amplitudes were very high in all three directions. Without good initialization, such levels are not accessible with only two volumes to register. The biomarkers on the one hand, and the artificial skin on the other hand were key to getting such results.

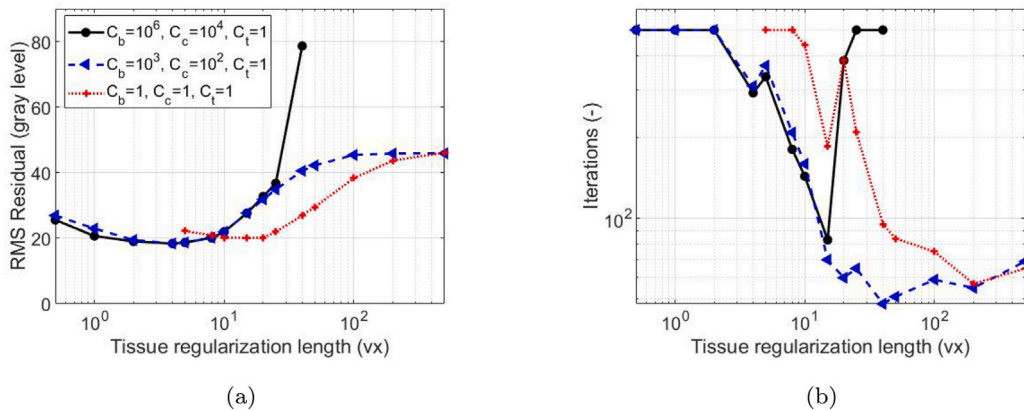
In the final step, DVC was run with the actual 3D images when initialized with the displacement field shown in Fig. 8 applying a contrast of  $C_b = 10^6$ ,  $C_c = 10^4$ ,  $C_t = 1$ . To probe the effect of regularization, the analysis was started with a large regularization length (*i.e.*,  $\ell_{\text{reg}} = 40$  vx). Once convergence was achieved, a new analysis was run with a lower regularization length (*i.e.*,  $\ell_{\text{reg}} = 20$  vx), and so on down to 0.5 vx. The upper bound was selected as higher values led to bad conditioning of the DVC Hessian matrix, especially when heterogeneous elastic contrasts were considered.

Fig. 9(a) shows the change of the RMS gray level residual as a function of the regularization length. There is a very significant decrease in RMS residual with  $\ell_{\text{reg}}$ , thereby indicating that results with large regularization lengths should not be kept. This trend can be understood from the fact that body forces were not negligible for the tissue. In the present case, the penalty term follows the hypothesis of

vanishing body forces. This is not valid as the soft tissue deformed due to gravity contrary to the other phases, which are stiffer and do not deform. Therefore the penalty term should be as small as possible and very small regularization should be applied. Since the elastic contrasts were very high for the bone and cartilage, the regularization in the tissue was essentially vanishing for the lower regularization lengths. This trend was observed for the three considered contrasts. However, when  $C_b = 10^6$ ,  $C_c = 10^4$ ,  $C_t = 1$ , the residual significantly increased before the other two cases. This difference is due to the large value of regularization length of bone and cartilage, which degrades the conditioning of the Hessian matrices.

To analyze convergence of the DVC algorithm, the number of iterations to reach convergence is displayed in Fig. 9(b). As the regularization length was decreased, the number of iterations augmented for all the applied contrast triplets. This trend was expected as less and less weight (*i.e.*, smaller  $\ell_{\text{reg}}$ ) was put on the tissue phase. Given the complexity of the sought deformation and the fact that the gray level contrast was not very high, such trend was unavoidable. For regularization lengths less than 3 vx when  $C_b = 10^6$ ,  $C_c = 10^4$ ,  $C_t = 1$  (or 3 vx when  $C_b = 10^3$ ,  $C_c = 10^2$ ,  $C_t = 1$  and 8 vx when  $C_b = C_c = C_t = 1$ ), the number of iterations became very high (*i.e.*, convergence in terms of L2-norm of the displacement corrections less than  $10^{-2}$  vx was no longer satisfied before the maximum number of iterations was reached).

It is worth noting that to properly capture the inframammary fold (Fig. 11(d)), a significant number of iterations was needed when  $\ell_{\text{reg}} = 4$  vx (Fig. 9(b)), which led to a solution with one of the lowest RMS residuals (Fig. 9(a)) for the highest considered elastic contrast. Further convergence studies are shown in Appendix B. By introducing elastic contrast, it was also possible to lower the regularization length in the tissue (*i.e.*, 4 vx for  $C_b = 10^6$ ,  $C_c = 10^4$ ,  $C_t = 1$  instead of 20 vx for



**Fig. 9.** Convergence analysis. (a) RMS gray level residuals and (b) number of iterations of the DVC algorithm as functions of the regularization length  $\ell_{\text{reg}}$  for three different elastic contrast settings.

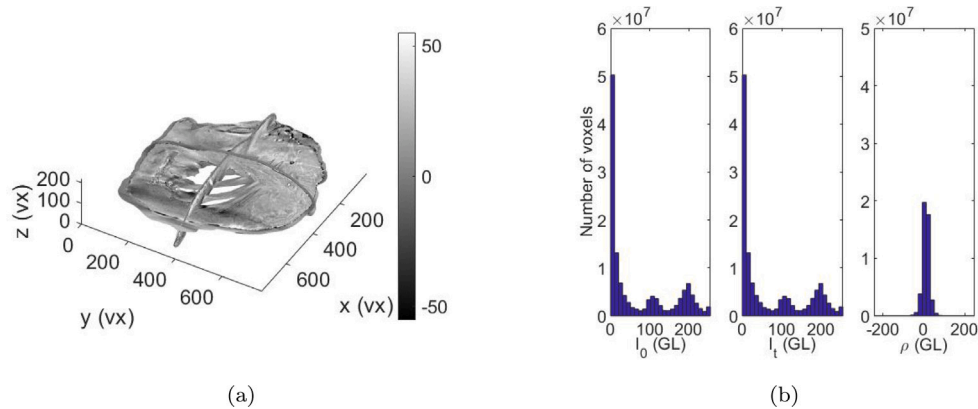


**Fig. 10.** (a) Gray level residuals for the last DVC analysis. (b) From left to right: gray level histograms of the reference volume  $I_0$ , deformed volume  $I_1$ , and DVC residuals  $\rho$  shown in sub-figure (a).

$C_b = 1$ ,  $C_c = 1$ ,  $C_t = 1$ ) to reach a lower final residual (18.3 instead of 20.2 gray level for homogeneous regularization). Introducing elastic contrast allowed for strongly penalizing the hard phase and limiting the regularization over the soft phase, which was therefore freer to move. All three convergence curves (Fig. 9(a)) have the same trend but higher contrasts allowed for significantly relaxing the constraints on the soft tissue.

From these two different quantities, the results obtained for a regularization length of 4 vx with heterogeneous regularization ( $C_b = 10^6$ ,  $C_c = 10^4$ ,  $C_t = 1$ ) were kept. 292 iterations were required to converge. The RMS residuals were equal to 18.3 gray levels (Fig. 10(a)). They were almost two times higher than those observed for the segmented volumes. However, given the fact that no special care was taken in the acquisition process, such levels are more than acceptable. Fig. 10(b) shows an almost centered distribution of the residuals with minimal bias, even though gray level conservation was not fully satisfied because of the followed acquisition protocol. As the scans were not acquired for DVC purposes, no effort was put into keeping the same filter values, which resulted in slightly different gray level distributions.

Fig. 11 shows the measured displacement field. Similarly to the results achieved with the segmented volumes, the tissue moved downward and created an inframammary fold (Fig. 11(d)). In all three directions, the displacement amplitudes were high (i.e., of the order of centimeters). The mask-based initialization allowed the DVC analysis to be started from a good initial guess, and the presence of gray level contrast in the phases gave more accurate and local information on

the displacement field (as an example, see  $u_z$  component in Figs. 8(c) and 11(c)).

The soft tissue experienced very large displacements, part of them due to rigid body motions (i.e., translations and rotations), but also to mechanical strains. In the present case, the Green-Lagrange strains ( $\mathbf{E} = \frac{1}{2}(\mathbf{F}^T \mathbf{F} - \mathbf{I})$ ) are reported. They were estimated from the exact differentiation of the shape functions of the 4-noded tetrahedra (i.e., T4 elements) to evaluate the deformation gradient tensor  $\mathbf{F}$ . Fig. 12 shows that the soft tissue underwent large strains (including shear in particular in the inframammary fold) up to 25% in magnitude, which is large between two scans only.

### 3.2. A posteriori uncertainty quantification

The DVC results obtained for a regularization length of 4 vx with  $C_b = 10^6$ ,  $C_c = 10^4$ ,  $C_t = 1$  led to residuals whose standard deviation was equal to 18.3 gray levels. With this information, the standard uncertainties  $\sigma$  were assessed *a posteriori* by varying the regularization length  $\ell_{\text{reg}}$ . Fig. 13(a) shows that the larger the regularization length, the lower the standard displacement uncertainty. This dependence illustrates the trade-off between measurement uncertainty and spatial resolution (here corresponding to the regularization length) (Leclerc et al., 2012; Taillandier-Thomas et al., 2014). The power law interpolation with exponent  $-1.5$  describes very well the reported results in accordance with the hypothesis of white Gaussian noise (Leclerc et al.,

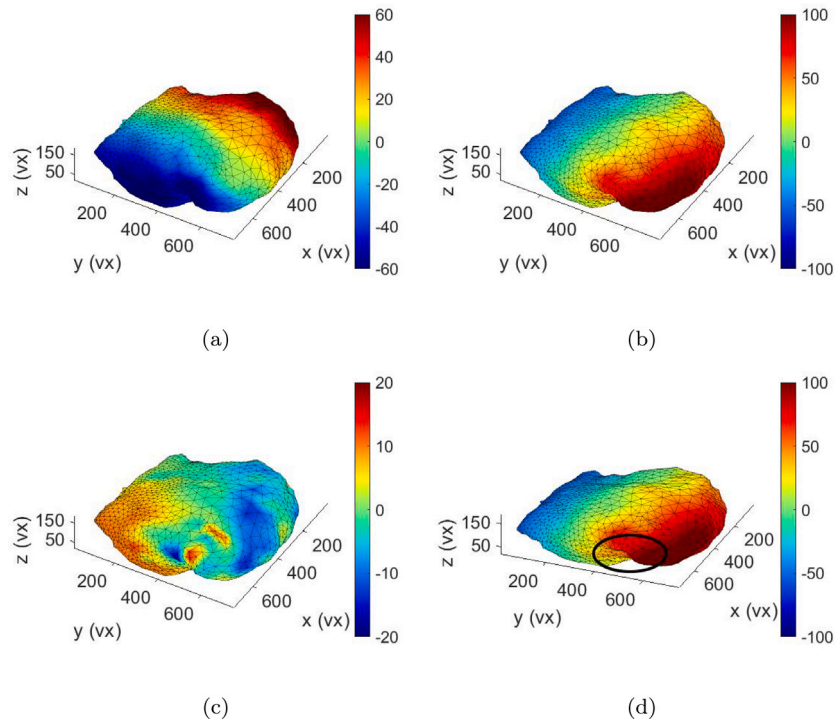


**Fig. 11.** Displacement fields expressed in voxels (1 vx  $\equiv$  0.34 mm) for the last DVC analysis displayed on the mesh without the outer skin layer. (a)  $u_x$ , (b)  $u_y$  and (c)  $u_z$  components plotted on the deformed mesh. (d)  $u_y$  component from another viewpoint to highlight the displacement discontinuity around the inframammary fold (black ellipse).

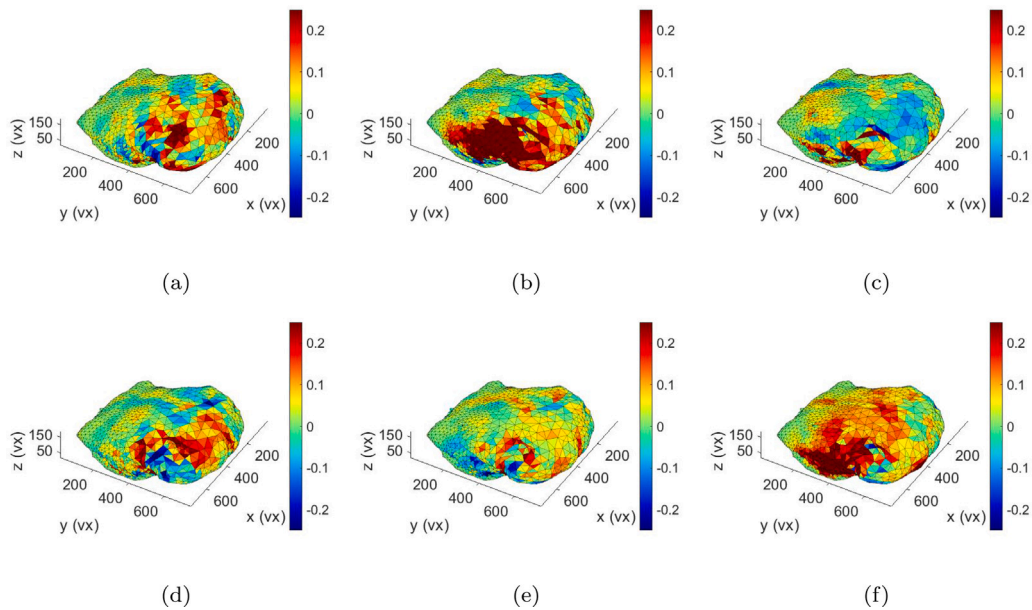


**Fig. 12.** Strain fields for the last DVC analysis displayed on the mesh without the skin layer. (a)  $E_{xx}$ , (b)  $E_{yy}$ , (c)  $E_{zz}$ , (d)  $E_{xy}$ , (e)  $E_{xz}$  and (f)  $E_{yz}$  components. The soft tissue underwent large strains (including shear in particular in the inframammary fold) up to 25% in magnitude.



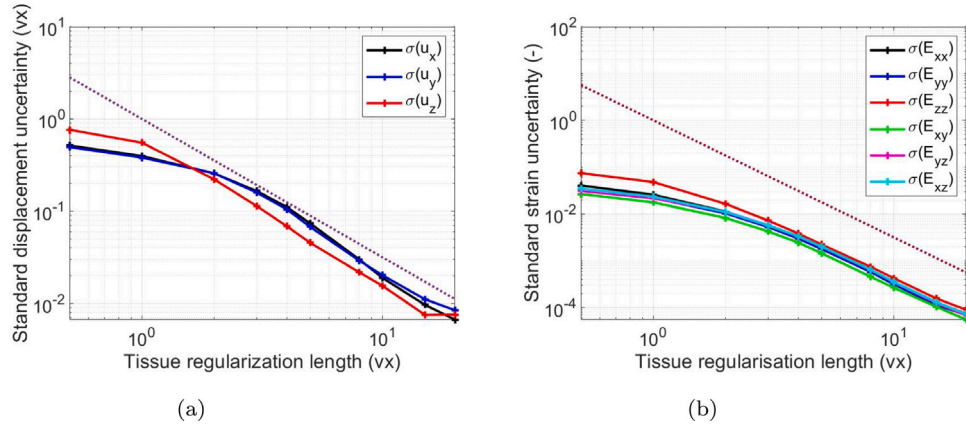


Fig. 13. Standard displacement (a) and strain (b) uncertainties as functions of the regularization length  $\ell_{\text{reg}}$  for an elastic contrast of  $C_b = 10^6$ ,  $C_c = 10^4$  and  $C_t = 1$ . The dashed lines show power law interpolations with exponent  $-1.5$  for the displacements (a) and  $-2.5$  for the strains (b).

Table 1

RMSE computed between the DVC deformed surface and the corresponding segmented surface. The data in parentheses correspond to homogeneous regularization and the other ones to the highest elastic contrasts.

Phase	RMSE (mm)
Soft tissue	2.2 (2.3)
Cartilage	3.1 (3.2)
Bones	2.6 (2.7)

2011, 2012). Similarly, the standard strain uncertainties also follow very closely a power law with exponent  $-2.5$  (Fig. 13(b)).

With the selected regularization length ( $\ell_{\text{reg}} = 4$  vx) and elastic contrasts ( $C_b = 10^6$ ,  $C_c = 10^4$ ,  $C_t = 1$ ), the standard displacement uncertainties were of the order of 0.1 vx, and the corresponding standard strain uncertainties were less than  $5 \times 10^{-3}$ . These levels are deemed sufficiently low in comparison to the reported results (Figs. 11 and 12).

### 3.3. Further validation

Last, the overall shape of the sample was well recovered (Fig. 14). In addition to the gray level residuals, in Table 1 the RMSE (Eq. (10)) was used as a metric for evaluating the trustworthiness of surface displacements. The measured error was a few millimeters (between 2.2 to 3.1 mm, which corresponds to a range of 6.8 to 9.4 vx). When the highest elastic contrasts were considered, all errors decreased about 0.1 mm in comparison to homogeneous regularization, which further validates their use. As the error was lower than the mean element size (i.e., 10 vx) and the mean spatial resolution (i.e., 17 vx), the measured displacement field was very realistic. It is worth remembering that this error included those due to the segmentation steps. As this multiphase sample had a complex morphology, and internal gray level contrast, the segmentation relied on coupling of growing from seeds algorithms, and smoothing with operator-dependent steps. The latter ones explain parts of the observed mismatches.

### 4. Conclusion

The objective of this work was to demonstrate the feasibility of using DVC to measure large biomechanical deformations. More specifically, the displacement field was measured for a breast subjected to gravity in two different positions when imaged via computed tomography. To obtain satisfactory results, a three-step DVC pipeline was implemented. The first step consisted in determining the motions of 15 biomarkers, which corresponds to one of the current clinical practices. It was shown that these motions were not sufficient to properly map the whole deformation field of the breast. The second step used the

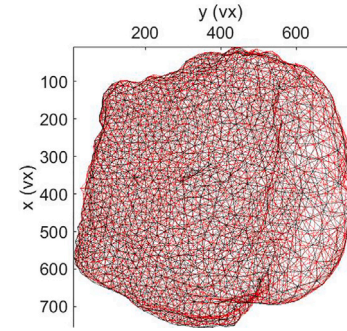


Fig. 14. Superposition of the deformed mesh resulting from DVC (red) with the expected mesh obtained from the segmentation of the deformed configuration (black).

previous initial guess to assess breast deformation with segmented volumes in which the three phases (i.e., bone, cartilage and soft tissue) were distinguished. An external skin was added to allow for the inframammary fold to be better captured. With these new motions, a final set of DVC analyses was performed on the original reconstructed volumes accounting for elastic contrasts in the three phases.

The results of this proof of concept study highlighted the efficiency of the DVC technique for a breast including the inframammary fold. Elastic contrasts were set according to literature data. The studied breast had regions with very high elastic contrast ( $10^6$  between bones and tissue, and  $10^4$  for cartilage), which was accounted for in the regularized DVC scheme used herein. Few DVC iterations were needed to quickly pre-converge to a suitable displacement field with a low RMS residual. The convergence study wrt. the regularization length showed that a rather low value could be chosen to obtain accurate results. If the regularization length was too large, meaningful displacement fluctuations were filtered out. Conversely, when the regularization length was too small, then convergence issues arose. Similar trends were observed for two other sets of elastic contrasts, thereby showing that the higher the contrast, the lower the regularization length (i.e., having a higher contrast, less regularization was applied to the soft tissue leading to lower registration residuals).

The present study had several limitations. First, the tomographic acquisitions were not optimal for DVC purposes. In particular, no repeat scans were performed for uncertainty quantifications. As only two scans were available, an *a posteriori* route was followed to assess standard kinematic uncertainties. Furthermore, CT-scans (but MRIs) are generally not used in clinical applications. Therefore, further studies are needed to investigate the feasibility of the present DVC pipeline when applied to MRIs. Second, the experiment was carried out on

an *ex vivo* injected cadaverous breast to be close to *in vivo* testing conditions. Therefore, this study may be extended to living tissues. It is hypothesized that blood flow between various acquisitions may impact the resulting gray levels and thus DVC results. This study also had user-dependent steps to be followed. The segmentation was manually assessed and the biomarker positions were assessed from their segmentation. For the patient geometry, some uncertainties and mismatches were observed between the gray level images and the associated segment (*i.e.*, the mesh needed sufficiently regular elements and simplifications of the geometry, namely, smoothing and simplification of the regions were necessary). Future studies are needed to automate these steps to reduce likely user-impact on the results.

Last, the results obtained herein may then be used in a calibration pipeline to get patient-specific material parameters. As the displacement field was computed for a finite element (FE) discretization, links with finite element simulations are straightforward. One would be able to predict the deformation of the organ in surgical positions. The DVC analysis may also be coupled with finite element analyses in cases of (self-)contact. The computed FE displacement field may then serve as initialization for DVC registrations. Its trustworthiness would then be probed thanks to the gray level residuals.

#### CRedit authorship contribution statement

**T. Lavigne:** Writing – review & editing, Writing – original draft, Visualization, Methodology, Investigation, Conceptualization. **A. Mazier:** Writing – original draft, Supervision, Data curation. **A. Perney:** Methodology. **S.P.A. Bordas:** Writing – review & editing, Supervision, Funding acquisition. **F. Hild:** Writing – review & editing, Writing – original draft, Software, Resources, Methodology, Investigation, Formal analysis, Conceptualization. **J. Lengiewicz:** Writing – original draft, Visualization, Supervision, Methodology, Investigation, Conceptualization.

#### Declaration of competing interest

The authors declare that they have no known competing financial interests or personal relationships that could have appeared to influence the work reported in this paper.

#### Data availability

The authors do not have permission to share data.

#### Acknowledgments

This study was supported by the European Union's Horizon 2020 research and innovation program under grant agreement No 811099, the Marie Skłodowska-Curie, Luxembourg grant agreement No. 764644, and the FNR Project No. C20/MS/14782078/QuaC. JL would like to acknowledge the support from EU Horizon 2020 Marie Skłodowska Curie Individual Fellowship MORPhEM under Grant 800150. The medical images used in the present study were obtained at Hopital Arnaud de Villeneuve, Département de Gynécologie Obstétrique in collaboration with Dr. Gauthier Rathat, Prof. Guillaume Captier, and AnatoScope. The authors would like to thank Synopsys for its support in providing access to the Simpleware software to generate the meshes used in this project, and RX-Solutions for their support and answers about the machine settings that were used. Last, the authors sincerely thank the person who donated her body to science so that anatomical research could be performed.

#### Appendix A. DVC hardware parameters

Orientation	−60°	−45°
Tomograph	EasyTom 150 (RX Solution)	EasyTom 150 (RX Solution)
Target/Anode	W (reflection mode)	W (reflection mode)
Voltage	120 kV	120 kV
Current	202 $\mu$ A	202 $\mu$ A
Focal spot size	50 $\mu$ m	50 $\mu$ m
Tube to detector	610 mm	610 mm
Tube to object	430 mm	430 mm
Detector	Varian 25 $\times$ 20 cm	Varian 25 $\times$ 20 cm
Definition	1920 $\times$ 1536 pixels	1920 $\times$ 1536 pixels
Projection definition	1840 $\times$ 728 pixels	1840 $\times$ 728 pixels
Number of projections	2111	1407
Angular amplitude	360°	360°
Frame average	15 per projection	15 per projection
Frame rate	30 fps	30 fps
Acquisition duration	28 min 08 s	18 min 40 s
Reconstruction algorithm	Filtered back-projection	Filtered back-projection
Filter	Tukey (75%)	Tukey (0%)
Gray levels amplitude	8 bits	8 bits
Volume size	768 $\times$ 781 $\times$ 216 voxels (after crop)	768 $\times$ 781 $\times$ 216 voxels (after crop)
Field of view	261.12 $\times$ 265.54 $\times$ 73.44 mm <sup>3</sup> (after crop)	261.12 $\times$ 265.54 $\times$ 73.44 mm <sup>3</sup> (after crop)
Image scale	0.34 mm/voxel	0.34 mm/voxel

#### Appendix B. Convergence analysis

The deformed meshes obtained in the convergence analysis for homogeneous regularization (*i.e.*,  $C_b = C_c = C_t = 1$ , see red dotted curve of Fig. 9(a)), are displayed in Fig. B.15 when the regularization length was relaxed from an initially very high value ( $\ell_{\text{reg}} = 500$  vx) to a very small one ( $\ell_{\text{reg}} = 5$  vx). In the last case, virtually no regularization was applied. As shown in Fig. 9(a), the RMS residuals decreased with the regularization length. Fig. 9(b) shows that a high regularization may help to converge quickly but tends to an unsatisfactory solution for which the lower fold cannot be captured. When the regularization length was lowered, the fold was better recovered until a minimum length was reached (*i.e.*, about 10 vx in the present case, see Fig. B.15(e)). For low regularization lengths, the minimization procedure no longer converged (Fig. 9(b)) to a trustworthy solution. It is worth remembering that the main cause of the soft tissue to deform was due to gravity. Since mechanical regularization was based on minimizing the equilibrium gap, its weight should not be too high to avoid nonphysical solutions. The results shown hereafter illustrate this phenomenon.

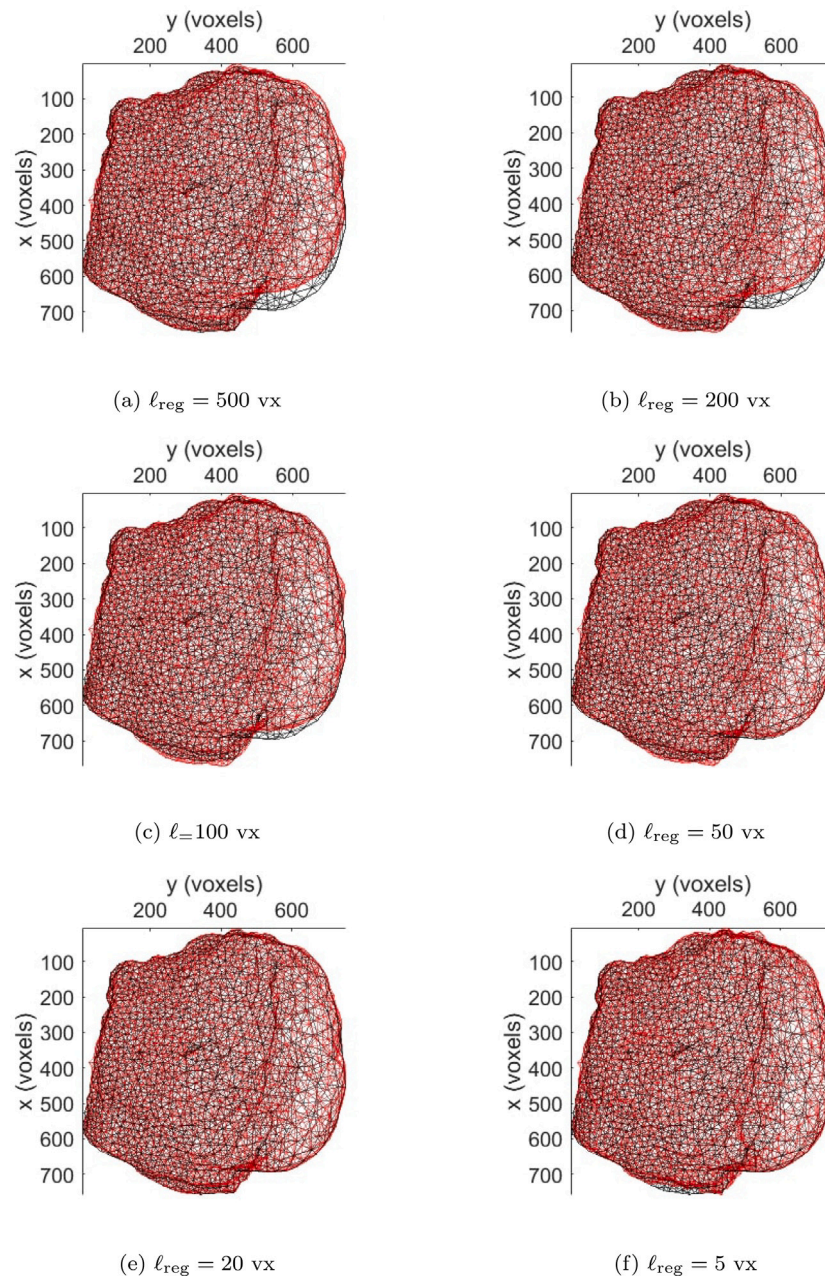


**Fig. B.15.** Evolution of the deformed mesh with the regularization length. Segmentation results are in a black wireframe and the DVC results are in red. (a)  $\ell_{\text{reg}} = 500 \text{ vx}$ , (b)  $\ell_{\text{reg}} = 200 \text{ vx}$ , (c)  $\ell_{\text{reg}} = 100 \text{ vx}$ , (d)  $\ell_{\text{reg}} = 50 \text{ vx}$ , (e)  $\ell_{\text{reg}} = 20 \text{ vx}$  and (f)  $\ell_{\text{reg}} = 5 \text{ vx}$ .

## References

- Bay, B., 2008. Methods and applications of digital volume correlation. *J. Strain Anal.* 43, 745–760.
- Bay, B., Smith, T., Fyhrle, D., Saad, M., 1999. Digital volume correlation: three-dimensional strain mapping using X-ray tomography. *Exp. Mech.* 39, 217–226.
- Benoit, A., Guérard, S., Gillet, B., Guillot, G., Hild, F., Mitton, D., Périé, J.-N., Roux, S., 2009. 3D analysis from micro-MRI during in situ compression on cancellous bone. *J. Biomech.* 42, 2381–2386.
- Besl, P.J., McKay, N.D., 1992. A method for registration of 3-D shapes. *IEEE Trans. Pattern Anal. Mach. Intell.* 14 (2), 239–256. <http://dx.doi.org/10.1109/34.121791>.
- Buljac, A., Jailin, C., Mendoza, A., Neggers, J., Taillandier-Thomas, T., Bouterf, A., Smaniotto, B., Hild, F., Roux, S., 2018a. Digital volume correlation: Review of progress and challenges. *Exp. Mech.* 58 (5), 661–708. <http://dx.doi.org/10.1007/s11340-018-0390-7>.
- Buljac, A., Taillandier-Thomas, T., Helfen, L., Morgeneyer, T., Hild, F., 2018b. Evaluation of measurement uncertainties of digital volume correlation applied to laminography data. *J. Strain Anal. Eng. Des.* 53, 49–65.
- Claire, D., Hild, F., Roux, S., 2004. A finite element formulation to identify damage fields: The equilibrium gap method. *Internat. J. Numer. Methods Engrg.* 61 (2), 189–208.
- Dall'Ara, E., Bodey, A., Isaksson, H., Tozzi, G., 2022. A practical guide for in situ mechanical testing of musculoskeletal tissues using synchrotron tomography. *J. Mech. Behav. Biomed. Mater.* 133, 105297. <http://dx.doi.org/10.1016/j.jmbbm.2022.105297>, URL: <https://www.sciencedirect.com/science/article/pii/S1751616122002107>.
- DeSantis, C.E., Ma, J., Gaudet, M.M., Newman, L.A., Miller, K.D., Sauer, A.G., Jemal, A., Siegel, R.L., 2019. Breast cancer statistics, 2019. *CA: Cancer J. Clin.* 69 (6), 438–451. <http://dx.doi.org/10.3322/caac.21583>.
- Disney, C.M., Eckersley, A., McConnell, J.C., Geng, H., Bodey, A.J., Hoyland, J.A., Lee, P.D., Sherratt, M.J., Bay, B.K., 2019. Synchrotron tomography of intervertebral disc deformation quantified by digital volume correlation reveals microstructural influence on strain patterns. *Acta Biomater.* 92, 290–304. <http://dx.doi.org/10.1016/j.actbio.2019.05.021>.
- Disney, C.M., Lee, P.D., Hoyland, J.A., Sherratt, M.J., Bay, B.K., 2018. A review of techniques for visualising soft tissue microstructure deformation and quantifying strain ex vivo. *J. Microsc.* 272 (3, SI), 165–179. <http://dx.doi.org/10.1111/jmi>.



- 12701, 5th Annual Symposium on Tomography for Scientific Advancement (ToScA), Univ Portsmouth, Portsmouth, ENGLAND, 2017.
- Disney, C.M., Mo, J., Eckersley, A., Bodey, A.J., Hoyland, J.A., Sherratt, M.J., Pitsillides, A.A., Lee, P.D., Bay, B.K., 2022. Regional variations in discrete collagen fibre mechanics within intact intervertebral disc resolved using synchrotron computed tomography and digital volume correlation. *Acta Biomater.* 138, 361–374. <http://dx.doi.org/10.1016/j.actbio.2021.10.012>.
- Duraes, M., Crochet, P., Pagès, E., Grauby, E., Lasch, L., Rebel, L., Van Meer, F., Rathat, G., 2019. Surgery of nonpalpable breast cancer: First step to a virtual per-operative localization? First step to virtual breast cancer localization. *Breast J.* 25 (5), 874–879. <http://dx.doi.org/10.1111/tbj.13379>.
- Eiben, B., Vavourakis, V., Hipwell, J.H., Kabus, S., Lorenz, C., Buelow, T., Williams, N.R., Keshtgar, M., Hawkes, D.J., 2016. Surface driven biomechanical breast image registration. In: Webster, R.J., Yaniv, Z.R. (Eds.), *Medical Imaging 2016: Image-Guided Procedures, Robotic Interventions, and Modeling*, Vol. 9786. International Society for Optics and Photonics, SPIE, pp. 282–291. <http://dx.doi.org/10.1117/12.2216728>.
- Fedorov, A., Beichel, R., Kalpathy-Cramer, J., Finet, J., Fillion-Robin, J.-C., Pujol, S., Bauer, C., Jennings, D., Fennessy, F., Sonka, M., Buatti, J., Aylward, S., Miller, J.V., Pieper, S., Kikinis, R., 2012. 3D slicer as an image computing platform for the quantitative imaging network. *Magn. Reson. Imaging* 30 (9), 1323–1341. <http://dx.doi.org/10.1016/j.mri.2012.05.001>.
- Forman, J.L., Kent, R.W., 2011. Modeling costal cartilage using local material properties with consideration for gross heterogeneities. *J. Biomech.* 44 (5), 910–916. <http://dx.doi.org/10.1016/j.jbiomech.2010.11.034>.
- Gavaghan, D.J., Whiteley, J.P., Chapman, S.J., Brady, J.M., Pathmanathan, P., 2008. Predicting tumor location by modeling the deformation of the breast. *IEEE Trans. Biomed. Eng.* 55 (10), 2471–2480. <http://dx.doi.org/10.1109/TBME.2008.925714>.
- Georgii, J., Paetz, T., Harz, M., Stoecker, C., Rothgang, M., Colletta, J., Schilling, K., Schlooz-Vries, M., Mann, R.M., Hahn, H.K., 2016. Simulation and visualization to support breast surgery planning. In: Tingberg, A., Lång, K., Timberg, P. (Eds.), *Breast Imaging*. Springer International Publishing, Cham, pp. 257–264.
- Gillard, F., Boardman, R., Mavrogordato, M., Hollis, D., Sinclair, I., Pierron, F., Browne, M., 2014. The application of digital volume correlation (DVC) to study the microstructural behaviour of trabecular bone during compression. *J. Mech. Behav. Biomed. Mater.* 29, 480–499. <http://dx.doi.org/10.1016/j.jmbbm.2013.09.014>, URL: <https://www.sciencedirect.com/science/article/pii/S1751616113003159>.
- Griffin, M., O'Toole, G., Sabbagh, W., Szarko, M., Butler, P., 2020. Comparison of the compressive mechanical properties of auricular and costal cartilage from patients with microtia. *J. Biomech.* 103, 109688. <http://dx.doi.org/10.1016/j.jbiomech.2020.109688>.
- Hild, F., Bouterf, A., Chamoin, L., Mathieu, F., Neggers, J., Pled, F., Tomićević, Z., Roux, S., 2016. Toward 4D mechanical correlation. *Adv. Mech. Simul. Eng. Sci.* 3 (1), 1–26.
- Hild, F., Bouterf, A., Roux, S., 2015. Damage measurements via DIC. *Int. J. Fract.* 191 (1–2), 77–105.
- Hild, F., Roux, S., 2012. Digital image correlation. In: Rastogi, P., Hack, E. (Eds.), *Optical Methods for Solid Mechanics. A Full-Field Approach*. Wiley-VCH, Weinheim (Germany), pp. 183–228.
- Hunt, K.D., O'Loughlin, V.D., Fitting, D.W., Adler, L., 1998. Ultrasonic determination of the elastic modulus of human cortical bone. *Med. Biol. Eng. Comput.* 36 (1), 51–56. <http://dx.doi.org/10.1007/bf02522857>.
- Hussein, A.I., Barbone, P.E., Morgan, E.F., 2012. Digital volume correlation for study of the mechanics of whole bones. *Procedia IUTAM* 4, 116–125. <http://dx.doi.org/10.1016/j.piutam.2012.05.013>.
- Huwe, L.W., Brown, W.E., Hu, J.C., Athanasiou, K.A., 2018. Characterization of costal cartilage and its suitability as a cell source for articular cartilage tissue engineering. *J. Tissue Eng. Regen. Med.* 12 (5), 1163–1176. <http://dx.doi.org/10.1002/term.2630>.
- Khatam, H., Reece, G.P., Fingeret, M.C., Markey, M.K., Ravi-Chandar, K., 2015. In-vivo quantification of human breast deformation associated with the position change from supine to upright. *Med. Eng. Phys.* 37 (1), 13–22. <http://dx.doi.org/10.1016/j.medengphys.2014.09.016>.
- Leclerc, H., Périé, J., Hild, F., Roux, S., 2012. Digital volume correlation: What are the limits to the spatial resolution? *Mech. Ind.* 13, 361–371.
- Leclerc, H., Périé, J., Roux, S., Hild, F., 2011. Voxel-scale digital volume correlation. *Exp. Mech.* 51 (4), 479–490.
- Lee, A.W.C., Schnabel, J.A., Rajagopal, V., Nielsen, P.M.F., Nash, M.P., 2010. Breast image registration by combining finite elements and free-form deformations. In: Martí, J., Oliver, A., Freixenet, J., Martí, R. (Eds.), *Digital Mammography*. Springer Berlin Heidelberg, Berlin, Heidelberg, pp. 736–743.
- Liu, L., Morgan, E.F., 2007. Accuracy and precision of digital volume correlation in quantifying displacements and strains in trabecular bone. *J. Biomech.* 40 (15), 3516–3520. <http://dx.doi.org/10.1016/j.jbiomech.2007.04.019>.
- Mazier, A., Ribes, S., Gilles, B., Bords, S.P., 2021. A rigged model of the breast for preoperative surgical planning. *J. Biomech.* 128, 110645. <http://dx.doi.org/10.1016/j.jbiomech.2021.110645>.
- Mendoza, A., Neggers, J., Hild, F., Roux, S., 2019. Complete mechanical regularization applied to digital image and volume correlation. *Comput. Methods Appl. Mech. Eng.* 355, 27–43.
- Meng, F., Chen, C., Hui, S., Wang, J., Feng, Y., Sun, C., 2019. Three-dimensional static optical coherence elastography based on inverse compositional Gauss-Newton digital volume correlation. *J. Biophotonics* 12 (9), e201800422. <http://dx.doi.org/10.1002/jbio.201800422>, URL: <https://onlinelibrary.wiley.com/doi/abs/10.1002/jbio.201800422>, arXiv:https://onlinelibrary.wiley.com/doi/pdf/10.1002/jbio.201800422.
- Míra, A., Carton, A.-K., Muller, S., Payan, Y., 2018. A biomechanical breast model evaluated with respect to MRI data collected in three different positions. *Clin. Biomech.* 60, 191–199. <http://dx.doi.org/10.1016/j.clinbiomech.2018.10.020>, URL: <https://www.sciencedirect.com/science/article/pii/S0268003318301426>.
- Nahas, A., Bauer, M., Roux, S., Boccara, A.C., 2013. 3D static elastography at the micrometer scale using full field OCT. *Biomed. Opt. Express* 4 (10), 2138. <http://dx.doi.org/10.1364/boe.4.002138>.
- Naylor, R., Hild, F., Fagiano, C., Hirsekorn, M., Renollet, Y., Tranquart, B., Baranger, E., 2019. Mechanically regularized FE DIC for heterogeneous materials. *Exp. Mech.* 59 (8), 1159–1170.
- Palanca, M., Oliviero, S., Dall'Ara, E., 2022. Microfe models of porcine vertebrae with induced bone focal lesions: Validation of predicted displacements with digital volume correlation. *J. Mech. Behav. Biomed. Mater.* 125, 104872. <http://dx.doi.org/10.1016/j.jmbbm.2021.104872>, URL: <https://www.sciencedirect.com/science/article/pii/S1751616121005087>.
- Palanca, M., Tozzi, G., Cristofolini, L., 2015. The use of digital image correlation in the biomechanical area: a review. *Int. Biomech.* 3 (1), 1–21. <http://dx.doi.org/10.1080/23355432.2015.1117395>.
- Payan, Y., Ohayon, J., 2017. Biomechanics of Living Organs: Hyperelastic Constitutive Laws for Finite Element Modeling. In: *Biomechanics of Living Organs*, Elsevier Science, URL: <https://books.google.fr/books?id=9WVJvgAACAAJ>.
- Peña Fernández, M., Sasso, S.J., McPhee, S., Black, C., Kanczler, J., Tozzi, G., Wolfram, U., 2022. Nonlinear micro finite element models based on digital volume correlation measurements predict early microdamage in newly formed bone. *J. Mech. Behav. Biomed. Mater.* 132, 105303. <http://dx.doi.org/10.1016/j.jmbbm.2022.105303>, URL: <https://www.sciencedirect.com/science/article/pii/S1751616122002168>.
- Pierce, E.L., Bloodworth, C.H., Naran, A., Easley, T.F., Jensen, M.O., Yoganathan, A.P., 2016. Novel method to track soft tissue deformation by micro-computed tomography: Application to the mitral valve. *Ann. Biomed. Eng.* 44 (7), 2273–2281. <http://dx.doi.org/10.1007/s10439-015-1499-9>.
- Rajagopal, V., 2007. Modelling Breast Tissue Mechanics Under Gravity Loading (Ph.D. thesis). URL: [http://www.esc.auckland.ac.nz/nash/publications/rajagopal\\_boundthesis\\_may2007\\_lowres.pdf](http://www.esc.auckland.ac.nz/nash/publications/rajagopal_boundthesis_may2007_lowres.pdf).
- Rajagopal, V., Nash, M.P., Highnam, R.P., Nielsen, P.M.F., 2008. The breast biomechanics reference state for multi-modal image analysis. In: Krupinski, E.A. (Ed.), *Digital Mammography*. Springer Berlin Heidelberg, Berlin, Heidelberg, pp. 385–392.
- Rajagopal, V., Nielsen, P., Nash, M., 2010. Modeling breast biomechanics for multi-modal image analysis-successes and challenges. *Wiley Interdiscip. Rev. Syst. Biol. Med.* 2, 293–304. <http://dx.doi.org/10.1002/wsbm.58>.
- Rankin, K., Steer, J., Paton, J., Mavrogordato, M., Marter, A., Worsley, P., Browne, M., Dickinson, A., 2020. Developing an analogue residual limb for comparative DVC analysis of transtibial prosthetic socket designs. *Materials* 13 (18), <http://dx.doi.org/10.3390/ma13183955>.
- Rho, J.Y., Ashman, R.B., Turner, C.H., 1993. Young's modulus of trabecular and cortical bone material: Ultrasonic and microtensile measurements. *J. Biomech.* 26 (2), 111–119. [http://dx.doi.org/10.1016/0021-9290\(93\)90042-d](http://dx.doi.org/10.1016/0021-9290(93)90042-d).
- Ruspi, M., Palanca, M., Faldini, C., Cristofolini, L., 2019. Full-field in vitro investigation of hard and soft tissue strain in the spine by means of digital image correlation. *Muscles Ligaments Tendons J.* 07 (04), 538. <http://dx.doi.org/10.32098/mltj.04.2017.08>.
- Santamaria, V.A.A., Garcia, M.F., Molimard, J., Avril, S., 2020. Characterization of chemoelastic effects in arteries using digital volume correlation and optical coherence tomography. *Acta Biomaterialia* 102, 127–137. <http://dx.doi.org/10.1016/j.actbio.2019.11.049>.
- Sartori, J., Kohring, S., Bruns, S., Moosmann, J., Hammel, J.U., 2021. Gaining insight into the deformation of achilles tendon entheses in mice. *Adv. Eng. Mater.* 23 (11, SI), <http://dx.doi.org/10.1002/adem.202100085>.
- Seedhom, B.B., Berry, E., Ostell, A.E., Cuppone, M., 2004. The longitudinal Young's modulus of cortical bone in the midshaft of human femur and its correlation with CT scanning data. *Calcified Tissue Int.* 74 (3), 302–309. <http://dx.doi.org/10.1007/s00223-002-2123-1>.
- Sutton, M., 2013. Computer vision-based, noncontacting deformation measurements in mechanics: A generational transformation. *Appl. Mech. Rev.* 65 (AMR-13-1009), 050802.
- Sutton, M., Orteu, J., Schreier, H., 2009. *Image Correlation for Shape, Motion and Deformation Measurements: Basic Concepts, Theory and Applications*. Springer, New York, NY (USA).
- Taillander-Thomas, T., Roux, S., Morgeneyer, T., Hild, F., 2014. Localized strain field measurement on laminography data with mechanical regularization. *Nucl. Inst. Methods Phys. Res. B* 324, 70–79.



- Tozzi, G., Dall'Ara, E., Palanca, M., Curto, M., Innocente, F., Cristofolini, L., 2017. Strain uncertainties from two digital volume correlation approaches in prophylactically augmented vertebrae: Local analysis on bone and cement-bone microstructures. *J. Mech. Behav. Biomed. Mater.* 67, 117–126. <http://dx.doi.org/10.1016/j.jmbbm.2016.12.006>, URL: <https://www.sciencedirect.com/science/article/pii/S1751616116304222>.
- Tsitova, A., Bernachy-Barbe, F., Bary, B., Dandachli, S.A., Bourcier, C., Smaniotto, B., Hild, F., 2021. Damage quantification via digital volume correlation with heterogeneous mechanical regularization: Application to an in situ meso-flexural test on mortar. *Exp. Mech.* <http://dx.doi.org/10.1007/s11340-021-00778-7>.
- Wu, D., Joffe, T., Mägi, C.Ö., Ferguson, S.J., Persson, C., Isaksson, P., 2022. A combined experimental and numerical method to estimate the elastic modulus of single trabeculae. *J. Mech. Behav. Biomed. Mater.* 125, 104879. <http://dx.doi.org/10.1016/j.jmbbm.2021.104879>, URL: <https://www.sciencedirect.com/science/article/pii/S1751616121005130>.